



Effect of the Outer Layer of Al Coatings Deposited by Cold Gas Spray on the Microstructure, Mechanical Properties and Corrosion Resistance of the AA 7075-T6 Aluminum Alloy

F. S. da Silva^{1,2} · N. Cinca² · S. Dosta² · I. G. Cano² · J. M. Guilemany² · A. V. Benedetti¹

Submitted: 16 October 2019 / in revised form: 9 March 2020 / Published online: 31 March 2020
© ASM International 2020

Abstract The corrosion of AA 7075-T6 aluminum alloy is a critical issue for many industries. In this study, aluminum coatings were deposited onto AA 7075-T6 by cold gas spray and the effect of the porous outer layer on different properties of the coating, including corrosion-resistance was investigated. As-prepared and polished samples were used to study the microstructure, morphology, mechanical properties and corrosion resistance of the coating in 3.5 wt.% NaCl solution. Cross-sectional analysis showed a dense structure, low porosity (0.8%) and thickness up to 300 μm ($\sim 100 \mu\text{m}$ for the porous outer layer and $\sim 200 \mu\text{m}$ for the compact inner layer). The sliding wear test resulted in a volume loss of $3.2 \times 10^{-4} \text{ mm}^3/\text{Nm}$ with an adhesive wear mechanism. The abrasive wear test showed a wear rate of $1.1 \times 10^{-4} \text{ mm}^3/\text{Nm}$ for the as-prepared coating and $0.8 \times 10^{-4} \text{ mm}^3/\text{Nm}$ for the polished coating. The as-prepared coating pores and interparticle spacing in the outer layer were mostly responsible for the increase in wear rate. For the polished coating immersed in 3.5 wt.% NaCl solution during 900 h, the electrolyte reached some specific points of the substrate as revealed by the cross-sectional analysis. Inspection of the as-prepared coating demonstrated that the coating/substrate interface

was completely damaged after long immersion times ($\sim 900 \text{ h}$).

Keywords AA 7075-T6 · aluminum · cold spray · corrosion · metal coatings · Thermal spray · wear

Introduction

Corrosion of aluminum alloys, particularly AA 7075-T6, is a critical issue for many industries, especially aircraft manufacture (Ref 1). This alloy is prone to localized corrosion (Ref 2, 3) and may be dissolved in different types of environments, such as those containing chloride ions (Ref 2). The mechanism of corrosion involves adsorption of chloride ions on the oxide film and their penetration through the film, leading to localized dissolution, blister formation and development of pits (Ref 4).

In order to protect Al alloys from localized corrosion, protective coatings must be used (Ref 5–10). The main function of the coatings is to isolate the substrate from the corrosive environment and consequently extend the lifetime of the material. Common protection methods for Al alloys involve the application of different types of coatings, using techniques such as electroless coating deposition (Ref 5), chromate coatings (Ref 6), organic coatings (Ref 7), hybrid coatings (Ref 8) and thermal spray coatings (Ref 9, 10). In the case of thermal spray coatings, the high spraying temperature attained in the plasma spray and high-velocity oxygen fuel (HVOF), processes hinder deposition onto Al and its alloys. The main reasons are the oxidation of the feedstock powder, high internal stresses and the multiphase structure of the deposited layers. The cold gas spray (CGS) technique operates with high kinetic and low thermal energy (Ref 9, 10), resulting in lower

Electronic supplementary material The online version of this article (<https://doi.org/10.1007/s11666-020-01023-8>) contains supplementary material, which is available to authorized users.

✉ A. V. Benedetti
benedeti@iq.unesp.br; assis.v.benedetti@unesp.br

¹ Institute of Chemistry, UNESP - São Paulo State University, Rua Prof. Francisco Degni 55, P.O. Box 355, Araraquara, SP 14800-060, Brazil

² CPT, Barcelona University, Martí I Franqués 1, 08028 Barcelona, Spain

residual stresses and reduced chemical transformations of the feedstock material (Ref 9, 10). Hence, the development of CGS has enabled avoidance of the drawbacks mentioned above due to its different technical features that modified the spray process. In CGS, a powdered raw material is heated at temperature $< 1000^{\circ}\text{C}$, which is low compared to conventional thermal spray technologies, and the feedstock powder is supersonically accelerated toward the substrate at rates between 500 and 1200 m s^{-1} depending on the deposition conditions (Ref 10, 11). Above a certain velocity, the impact of the particles causes intense plastic deformation of the powder and substrate (Ref 10). With the impact of subsequent particles, the coating builds up by means of a tamping effect (Ref 9–14). In the case of metallic coatings, adiabatic shear instabilities (ASIs) seem to be responsible for the bonding mechanism (Ref 10). The energy associated with the impact can even melt the particle shells, which greatly increases the bonds among the particles and between the particles and the substrate (Ref 10, 15). Furthermore, the lower density and high ductility of metals such as Al contribute to successful deposition onto various substrates (Ref 16–18).

As-prepared coatings produced by CGS technique tend to present a porosity gradient, with an inner dense region, a more porous outer region and a final rough surface finish, because of the incoming particles on densifying the previously deposited ones (Ref 10). The surface roughness is important for providing an ideal surface morphology for the adhesion of paints, sealants and top coatings. Removal of the top layer by polishing results in a smoothed coating surface and a compact microstructure like that of bulk Al. Several researchers have been describing the corrosion resistance and mechanical properties of as-prepared coatings (Ref 9–23). Some of the works have evaluated Al coatings (Ref 10, 11, 18, 19, 21, 23). These coatings were mainly evaluated by using polarization electrochemical techniques for short immersion times, being observed strong damage of the top layer and, in some cases, the coating/substrate interface. Wear studies showed that a combination of adhesive and abrasive wear is observed for Al coatings (Ref 12, 16–23). The volume loss and wear rate occur mainly due to the coatings defects, for instance, porosity, cracks and interparticle spacing (Ref 18–23). However, studies have shown that the wear rate can achieve low values due to the formation of oxides, which act as lubricant (Ref 18–23). None of these works compared the influence of outer and the inner layers on the mechanical properties and corrosion resistance of deposited Al powder onto AA 7075-T6 alloy. Therefore, the aim of this work was to investigate the influence of morphology and microstructure of as-prepared and polished coatings applied on AA 7075-T6 alloy, using the CGS technique, on

mechanical properties and corrosion resistance of the material.

Experimental

Feedstock Powders, Substrates and Reactants

Aluminum feedstock powders (99.7 wt.% Al) were produced by a gas atomization process and supplied by TLS Technik GmbH (Germany). The substrate used was AA 7075-T6 alloy with the following composition (in wt.%): 0.18 Cr, 2.1 Mg, 1.2 Cu, 5.1 Zn and balance Al. The Al powder was sprayed onto AA 7075-T6 coupons ($50\text{ mm} \times 20\text{ mm} \times 5\text{ mm}$ and $\varnothing = 25.4\text{ mm}$ and $h = 25.4\text{ mm}$). These were prepared by grinding using P240 SiC paper, which gave a surface roughness, R_a of $\sim 1\text{ }\mu\text{m}$, obtained as the average of at least ten roughness indentations on the sample surface. The measurements were performed using a Mitutuyo SurfTest 301 tester and a calibrated precision reference with roughness of $2.97\text{ }\mu\text{m}$. The electrolyte solution used during the corrosion tests was aqueous 3.5 wt.% NaCl (99.8%, Sigma-Aldrich) prepared according to ASTM D 1141-98. Keller's reagent (2 mL HCl, 1 mL HF, 3 mL HNO₃ and 90 mL H₂O) was used for etching the surface of the coating cross section.

Coating Preparation

The as-prepared Al coatings were obtained as described previously (Ref 18). Five layers were deposited, using the following spraying parameters: 25 bar pressure, $350\text{ }^{\circ}\text{C}$ gas temperature, traverse velocity 500 mm s^{-1} and 40 mm distance from the substrate. The polished coatings were obtained from the as-prepared coating by abrasion with P600, P1200 and P4000 SiC papers and followed by polishing with 1 and $0.5\text{ }\mu\text{m}$ diamond suspensions, resulting a final roughness (R_a) $\cong 0.5\text{ }\mu\text{m}$. Figure 1 shows photographs of the as-prepared ($R_a \cong 9.5\text{ }\mu\text{m}$) and polished coating ($R_a \cong 0.5\text{ }\mu\text{m}$) samples.

Structural and Morphological Analyses

The structures of the powder and coatings were investigated by x-ray diffraction (XRD), using a Siemens Model D5000 diffractometer. A JEOL JSM-5310 scanning electron microscope (SEM) coupled to an x-ray microanalysis (EDS) system was used to analyze the powders and coatings. Laser diffraction spectroscopy (LDS) was used to determine the particle size distribution of the powders. Cross-sectional SEM images and ImageJ software were used to determine the mean coating thickness (minimum of

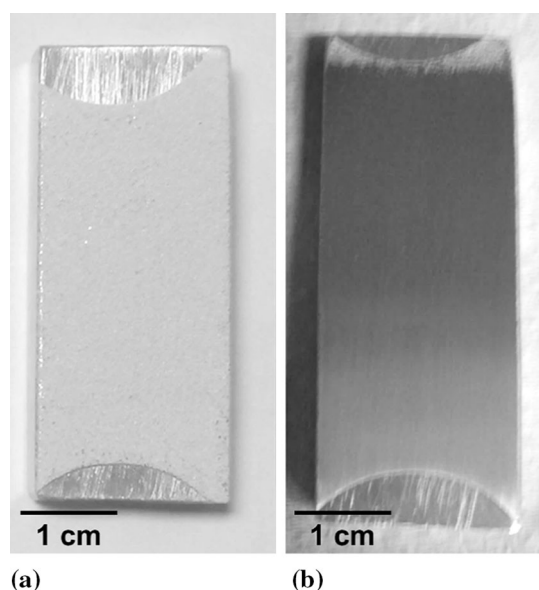


Fig. 1 (a) As-prepared coating and (b) polished coating

10 measurements) and porosity (at least 10 images) of the coatings, according to the ASTM E2109-01 method.

Adhesion, Hardness and Mechanical Testing of the Coatings

The tensile strength was evaluated according to the ASTM C-633 method, using at least three samples. The hardness values were determined using the polished cross sections of coatings and substrate, according to the ASTM E384-99 method.

The friction coefficients and wear rates of the samples were evaluated using ball-on-disk (BoD) tests, according to the ASTM G99-04 procedure, using a CM4 instrument. Steel balls 14 mm in diameter and with hardness (HVN_{300}) of 1700 were used as counter bodies with the following test parameters: sample relative velocity of 131 rpm, total test length of 1000 m, sliding speed of 0.029 m s^{-1} and load of 5 N. The wear paths were analyzed by SEM and confocal microscopy (Leica DCM 3D microscope), with the mass loss being determined from the volume removed.

Rubber wheel (RW) tests were performed according to ASTM G65 for both as-prepared ($R_a \approx 94 \mu\text{m}$) and polished samples ($R_a \approx 0.50 \mu\text{m}$). A rotation of 139 rpm, load of 20 N and flow of silica ($\varnothing = 0.4$ to 0.8 mm) between 250 and 310 g min^{-1} were the parameters used for the tests. The mass loss was measured every 1 min in the first 5 min and then every 5 min until the test was complete (30 min).

Corrosion Measurements

A Gamry Reference 600 system employed the electrochemical tests performed in aerated and unstirred 3.5% NaCl solution, at $25 \pm 1^\circ\text{C}$, using a three-electrode Tait-type cell (Ref 24). The reference electrode was $\text{Ag}|\text{AgCl}|\text{KCl}3\text{mol/L}$ coupled to a Luggin capillary, while the auxiliary electrode was a Pt mesh. The working electrode was the substrate or coated substrate, with 1 cm^2 exposed to the electrolyte. Open-circuit potential (E_{OCP}) and electrochemical impedance spectroscopy (EIS) measurements were performed to evaluate the corrosion resistance performance of the samples. The tests were conducted during 240 h for the AA 7075-T6 substrate and during ~ 900 h for the coatings.

EIS diagrams were obtained at 1 h and then every 24 h during the period of the experiment, in the frequency range from 100 kHz to 5 mHz, applying a sinusoidal potential perturbation of 10 mV rms on E_{OCP} and collecting 10 points/frequency decade. The Kramers–Kronig transform (KKT) was used to confirm the consistency of the experimental data. The EIS responses were quantitatively analyzed using electrical equivalent circuit (EEC) theory and Z-view[®] software.

Results and Discussion

Structure and Morphology of the Powders and Coatings

The powder presented a micrometer particle size with submicron particles (Fig. 2a) formed during solidification in the gas atomization process (Ref 25, 26). The morphology was rounded, incompletely spherical and without pores (Fig. 2a and insert). The particle size ranged from 9 to $52 \mu\text{m}$, with an average of $22 \mu\text{m}$ (Fig. 2b). These characteristics confirmed that the feedstock material possessed ideal size (1–50 μm) and morphology required for spraying by CGS (Ref 27). A smaller size and regular shape of the particles enable higher velocities to be achieved during the spraying process, so the particles reach the substrate with high kinetic energy, resulting in substantial plastic deformation and the production of dense and compact coatings (Ref 28).

The XRD patterns of the feedstock powders and coatings showed the same characteristic peaks (Fig. 3). Therefore, the compositions were similar, being homogeneous and almost oxide-free. The formation of new phases did not occur due to the high kinetic energy and low thermal energy inherent to the CGS technique (Ref 10, 28, 29).

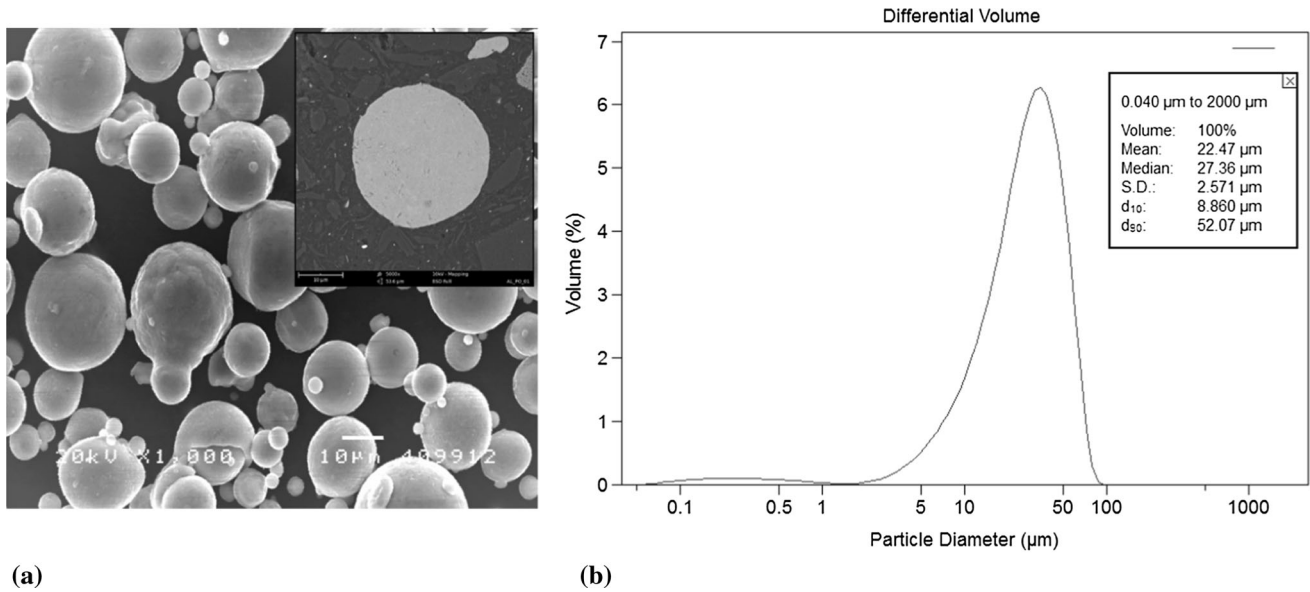


Fig. 2 (a) SEM images and (b) LDS plots for the feedstock powder

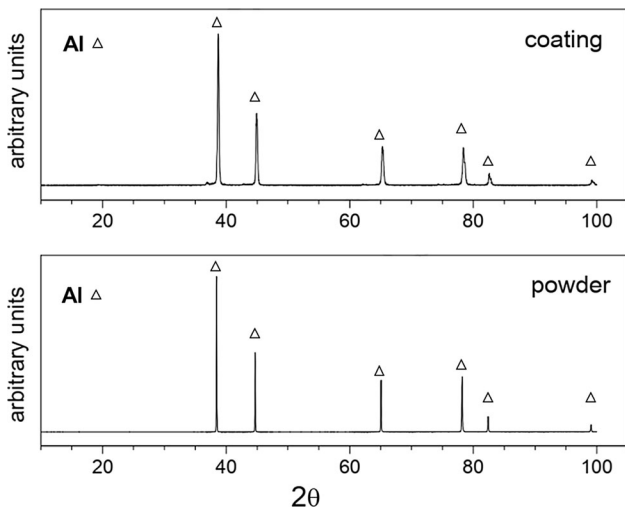


Fig. 3 X-ray diffractograms for powders and coatings

After etching treatment, the coating cross section showed a microstructure typical of CGS coatings, with the deformation of the particles (Fig. 4). Small defects (pores) were formed at boundaries of the particles along the coating cross section, mainly at the outer layer of the coating. These results agree with (Ref 18) that have described the CGS coatings as basically consisting of some pores in the top layer and a dense bottom layer.

The surface of the as-prepared coating presented a rough and irregular morphology, with the top layer being less compact than the bottom layer (Fig. 5a and b). This agreed with the literature (Ref 29–32) and reflected the accumulative densifying effect resulting from successively impacting particles. In the bottom layer, the deposit experienced an intensive tamping effect, with enough

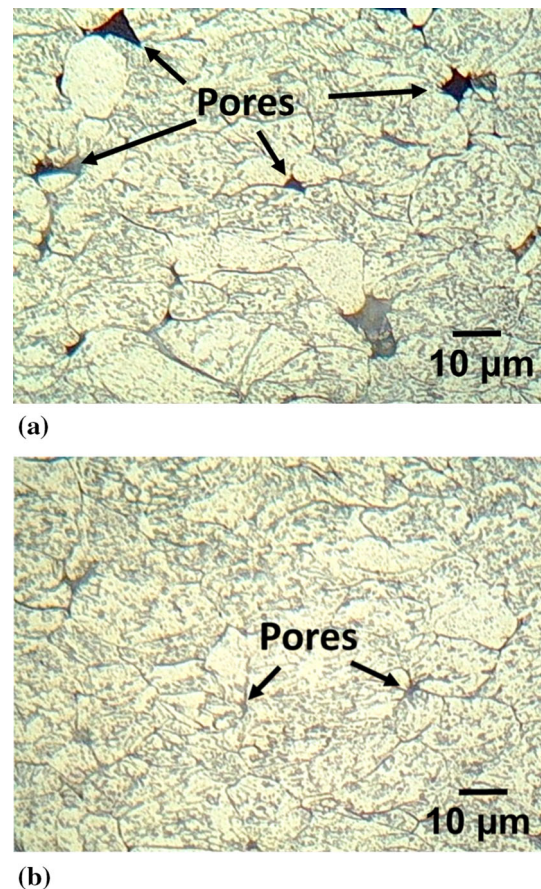


Fig. 4 Cross-sectional image of the (a) outer layer and (b) bottom layer after etching

deformation to decrease the porosity (Ref 28, 33). In the case of the polished coating, the cross-sectional microstructure was dense, with small pores (Fig. 5c and d),

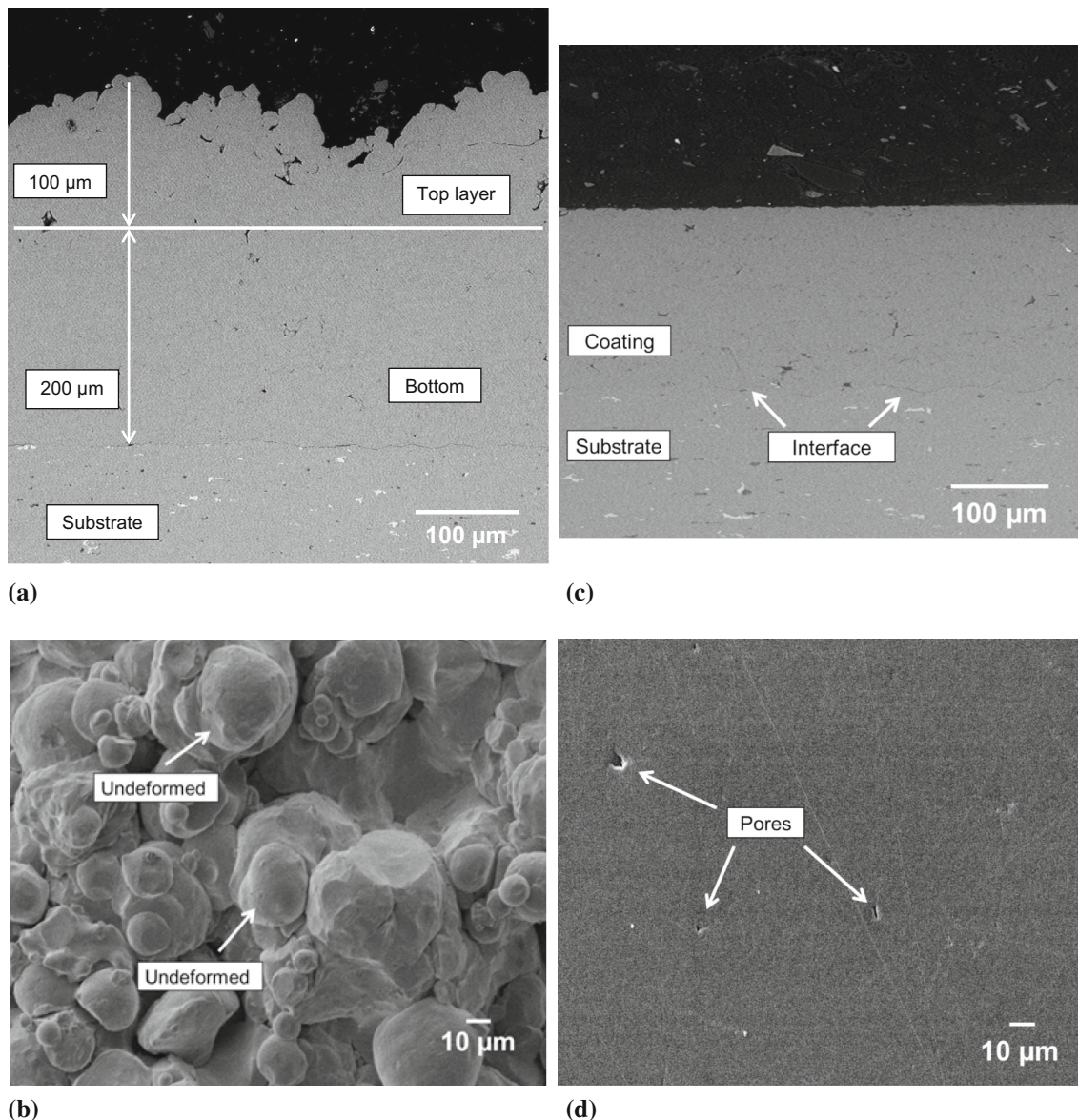


Fig. 5 SEM images of cross section and surfaces: (a) as-prepared coating cross section, (b) surface of as-prepared coating, (c) polished/coating cross section and (d) surface of polished coating

while the morphology of the surface was like that of the bulk Al (Fig. 5d). Both coatings showed porosity below 0.8%, indicating that a compact Al coating was obtained. The low microstructural porosity resulted from the accumulative effect of tamping by the successive impacts of arriving particles (Ref 33). The total thicknesses of the as-prepared and polished coatings were $309 \pm 12 \mu\text{m}$ and $204 \pm 4 \mu\text{m}$, respectively. Analysis of the coating cross section showed that the top layer was $\sim 100 \mu\text{m}$ thick, while the bottom layer was $\sim 200 \mu\text{m}$ thick (Fig. 5a). The coating/substrate interface was free from delamination (Fig. 5a and c). The adherence of the coating was $\approx 25 \text{ MPa}$, as determined using the ASTM C-633

procedure. Both the as-prepared and polished coatings failed at the substrate/coating interface, indicating that the interlayer bonding was stronger than that of the substrate/coating interface. The Vickers hardness values along the cross section were: $51 \pm 2 \text{ HV}_{100}$ outer layer, $58 \pm 1 \text{ HV}_{100}$ for the bottom layer and $162 \pm 3 \text{ HV}_{100}$ for AA7075-T6 substrate. The higher hardness value of the inner layer is assigned to the denser and compact microstructure of this region as shown in Fig. 4(b). The lower hardness values of the coatings compared to the substrate could be explained by the alloy composition and by the presence of micropores and interparticle boundaries

that affect the hardness and mechanical properties of the CGS coatings (Ref 20, 28).

Mechanical and Tribological Characterization

Ball-on-Disk Test

The friction wear resistance of the CGS coating was tested by applying a load of 5 N to the surfaces with initial roughness (R_a) of 0.8 μm . After the sliding wear test, the width of the wear track on the coating was 225 μm and the volume loss was $3.2 \times 10^{-4} \text{ mm}^3 \text{ N}^{-1} \text{ m}^{-1}$ (Table 1).

Figure 6 shows the wear paths on the coating after the test. The profiles of the wear paths (Fig. 6b) also provided evidence of the adhesive wear mechanism (Ref 18). The adherence of Al on the surface of steel ball (Fig. 6c) provided further evidence of the adhesive wear mechanism (Ref 18), while the ball showed virtually no wear, demonstrating that there was transfer of adhesive material from the softer coating to the harder counterpart. All these features were clear evidence of an adhesive wear mechanism. The appearance of the surface was indicative of adhesive wear (Ref 18, 34), and the outside of the path was characteristic of plowing and extrusion of the worn material (Ref 18, 34). The images showed that the coating material was plastically deformed during the test and that parts were transferred to the wear track edges. The loose wear debris had the same color and appearance as the coating material. Some small areas showed oxide formation, evidenced by EDS analysis (Fig. S1, SD) (Ref 18, 34, 35).

Rubber Wheel Test

For the as-prepared coating, the abrasive wear rate decreased slowly for short times (2–3 min) and then remained constant at $1.1 \times 10^{-4} \text{ mm}^3 \text{ N}^{-1} \text{ m}^{-1}$, while for the polished coating the abrasive wear rate was $0.8 \times 10^{-4} \text{ mm}^3 \text{ N}^{-1} \text{ m}^{-1}$ for all the testing time. The pores and interparticle spaces are considered preferential paths to initiate material loss in wear tests, increasing the wear rate (Ref 20). The lower number of pores and interparticle spaces (Figs. 4, 5) and consequently the higher hardness value of the bottom layer are the reasons for the

slight decrease in the mass loss of the polished coating. SEM images of the wear tracks (Fig. 7) showed an aspect of plowing and areas of different colors, indicating that oxides were formed during the wear test. The presence of Al oxides was corroborated by EDS analysis (Fig. S2, SD) of debris in some regions along the wear path. These oxides act as lubricants that reduce the rate of abrasive wear of the coating, hence explaining the low abrasive wear rate of the coatings (Ref 18, 36).

Corrosion Results

Open-Circuit Potential Results

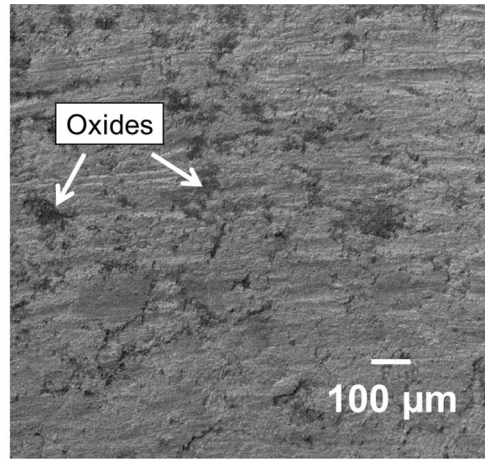
Figure 8 shows the evolution of E_{OCP} during the immersion of the samples in chloride solution for relatively long times of 240 h (AA 7075-T6 substrate), ~ 900 h (as-prepared coating) and ~ 900 h (polished coating). In the case of the substrate, E_{OCP} decreased from -0.64 V versus Ag/AgCl/KCl3mol/L to around -0.79 V versus Ag/AgCl/KCl3mol/L after 24 h of immersion, followed by a decrease to -0.92 V versus Ag/AgCl/KCl3mol/L, and then a slight increase to -0.87 V versus Ag/AgCl/KCl3mol/L occurs until the end of the test (240 h). The decrease in E_{OCP} was attributed to the dissolution of oxide previously formed on the surface and to the adsorption of Cl^- ions on the electrode (Ref 4, 18). The oscillation of E_{OCP} could be explained by dissolution/repassivation of the matrix around the intermetallic particles and/or dissolution of some phase from the matrix (for example a Mg-enriched phase) due to the galvanic couple effect (Ref 4, 18, 37).

The E_{OCP} for the polished coating was approximately -0.88 versus V/Ag/AgCl/KCl3mol/L independent of time, like the values obtained for the bulk aluminum in a chloride medium (Ref 32, 38). The E_{OCP} for the as-prepared coating showed variations of potential in a range no higher than 0.160 V (Fig. 8), which could be attributed to the diffusion of electrolyte through the pores of the top layer, the different concentration of oxygen in the bottom of the pores and pit formation/repassivation on the Al surface (Ref 4). Briefly, the corrosion mechanism involved the adsorption of chloride ions on the oxide film, their penetration through the film leading to localized dissolution at defects in the oxide, resulting in the formation of blisters and development of pits, initiating at the top of the as-prepared coating (Ref 18, 32). Cross-sectional SEM images (Figs. 9, 10) of the as-prepared coating after the E_{OCP} measurements showed that at the beginning of immersion, the pores at the top layer became larger due to the attack of Al by chloride ions (Ref 18), while the top layer of the coating, which was more porous, was completely full of defects and/or pits. The thicker aluminum particles were not corroded (Fig. 10), indicating that the pitting initiated

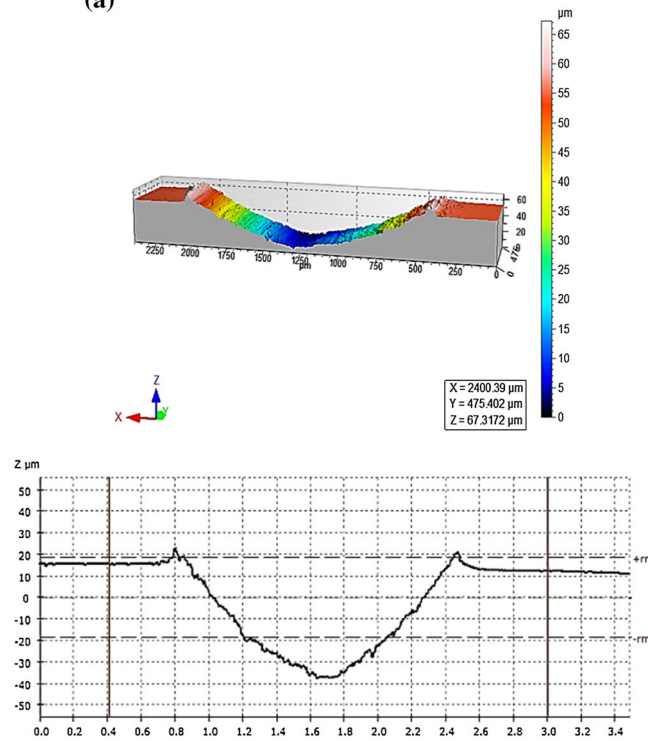
Table 1 Main wear properties of the Al CGS coating

Parameter	Coating
Friction coefficient	0.17
Volume lost ($\text{mm}^3 \text{ N}^{-1} \text{ m}^{-1}$)	3.2×10^{-4}
Wear track width (μm)	225

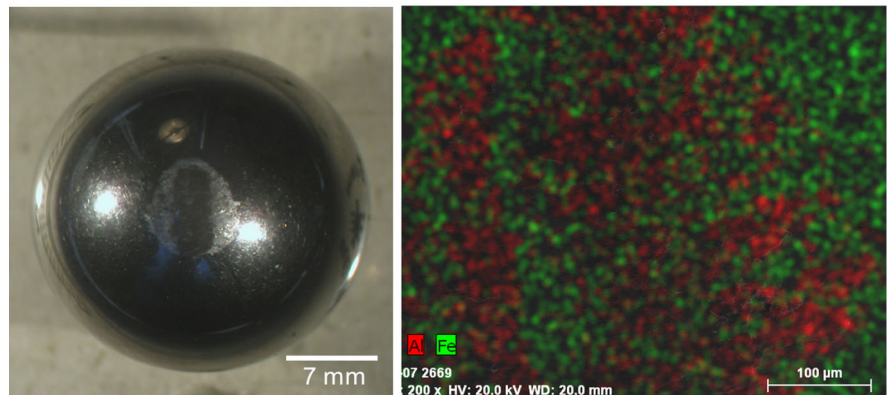
Fig. 6 (a) SEM image of the morphology of the wear paths on the as-prepared coating, (b) confocal microscopy image of the morphology of the wear paths on the as-prepared coating and (c) optical micrographs of steel ball after ball-on-disk test and EDS analysis of the surface of the ball



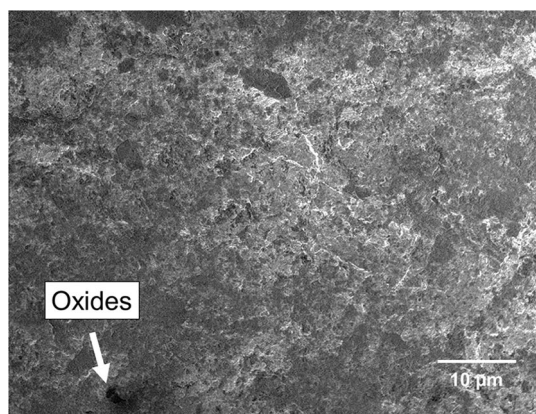
(a)



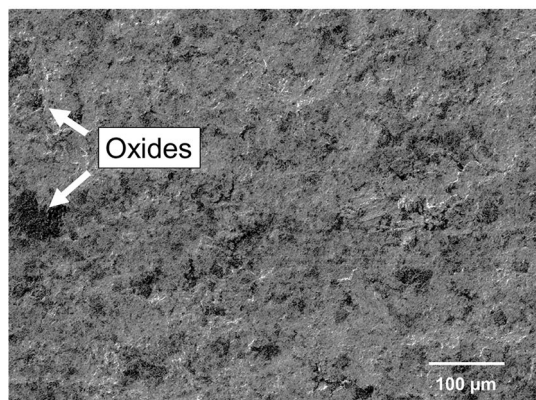
(b)



(c)



(a)



(b)

Fig. 7 Morphological features of the rubber wheel wear tracks: (a) as-prepared coating and (b) polished coating

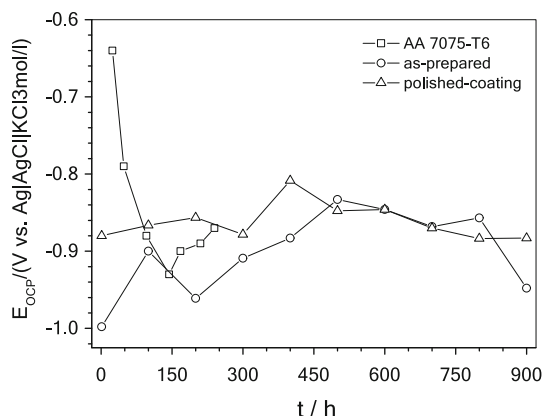


Fig. 8 E_{OCP} according to time for the samples immersed in aerated and unstirred 3.5 wt.% NaCl solution at 25 °C

at the borders of these particles, while there was dissolution of small particles, spread over the entire sample surface (Ref 18). The as-prepared coating showed pores at the bottom layer (Fig. 9), and the coating/substrate interface was completely damaged (Fig. 9). The polished coating showed pit formation and enlargement at the surface of the

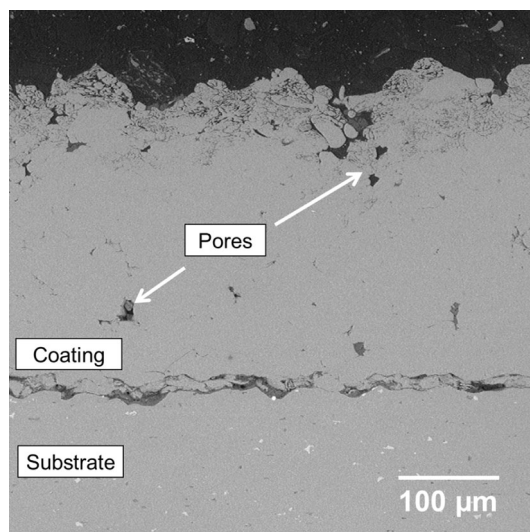


Fig. 9 SEM images of the as-prepared coating cross section after ~ 900 h of immersion in 3.5 wt.% NaCl

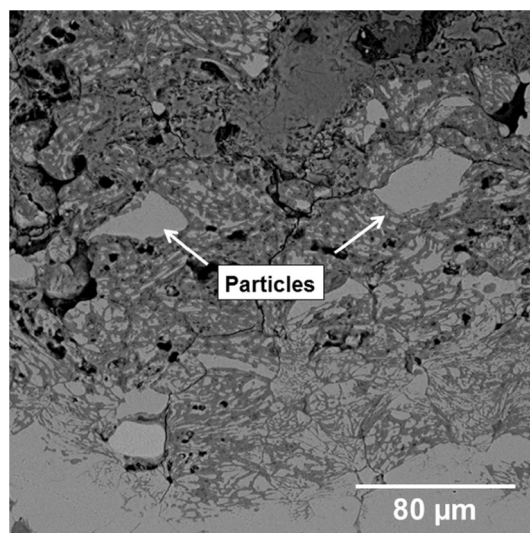


Fig. 10 Cross-sectional image of the top layer of the as-prepared coating after ~ 900 h in 3.5% NaCl

coating (Fig. 11), which was mainly prevalent in regions with microcracks or other small defects. The cross-sectional SEM images (Fig. 12) showed pathways in some specific areas, due to the initiation of the corrosion process at the borders of the coarse Al particles and dissolution of small particles as described previously. The top layer of the as-prepared coating appeared to be unable to improve the corrosion resistance for long immersion times, which was probably due to its inherent porous characteristic. The pores and defects at the top layer enabled the electrolyte to rapidly reach the bottom layer, indicating the poor barrier quality of the top layer. Subsequently, the formation of pits and pathways occurred due to the presence of small defects

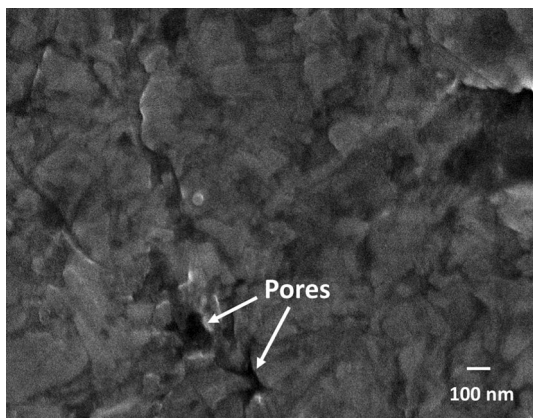


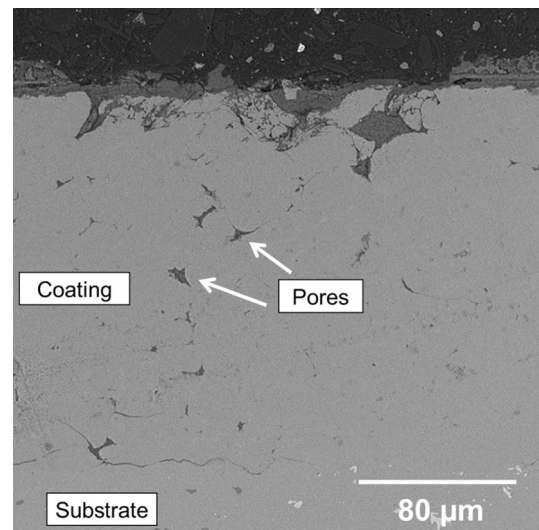
Fig. 11 Surface image of the polished coating after ~ 900 h in 3.5% NaCl

in the bottom layer that allowed the electrolyte to reach the coating/substrate interface.

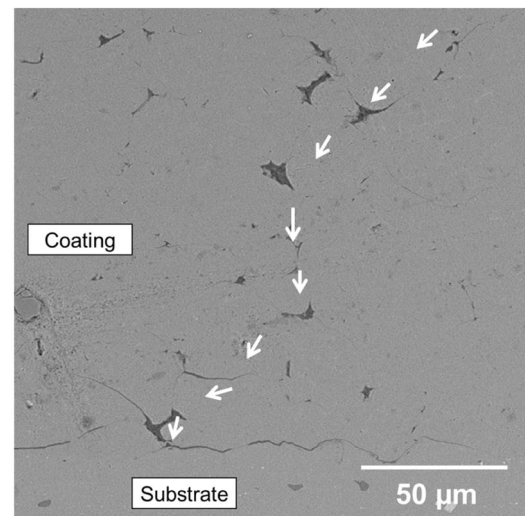
Studies showed that particles deposited by cold spraying undergo initial deformation on impact, resulting in their adherence to the particles deposited previously, followed by further deformation caused by the impacts of incoming particles, resulting in a tamping effect (Ref 39). This mechanism provides an explanation for the dense and compact coatings. Recent studies have been showed the reduction in microcracks and porous in the bottom layer of the coating (Ref 26, 40–43). The porosity of the coating decrease by spraying Al particles mixed with ceramic particles (Al-Al₂O₃, Al-SiC) (Ref 26, 39). The presence of the ceramic particles increases the tamping effect due the high hardness of ceramic particles increasing the plastic deformation of pre-deposited particles resulting in a denser and compact coating decreasing the rate of diffusion of aqueous solution through the coating and the corrosion. Thermal treatments after the spraying process also contributed to the decrease in corrosion (Ref 26). At lower heat-treating temperature, some diffusion between particles occurs (Ref 26, 41–43). For the porous coating, the interface between particles will become obscure for the dense coating and only the compactly connected interfaces disappear. Further increasing the heat-treating temperature, diffusion at the particle interfaces became more intense and the interfaces completely disappear (Ref 26, 41–43). In summary, heat treatment improves the bonding quality and diminishes interparticle boundaries, which are preferential sites for corrosion. Moreover, the heat treatment decreases the coating porosity and increases the coating barrier effect.

EIS Results

Figures 13 and 14 show representative impedance diagrams for the Al coatings, while Fig. S3 (SD) shows the



(a)



(b)

Fig. 12 Cross-sectional SEM images of the polished coating after 900 h of immersion in 3.5 wt.% NaCl: (a) coating cross section, and (b) bottom layer with coating/substrate interface

corresponding diagrams for the substrate in NaCl solution, as a function of immersion time. The impedance results for each coating (> 10 diagrams/coating) were recorded throughout the period, and the results obtained at ~ 70 h and ~ 500 h were used to represent the set of experiments. In Figs. 13 and 14, the symbols correspond to the experimental impedance data and the solid lines are the fits.

After 1 h of immersion, the Nyquist plot for the substrate apparently showed two time constants (Fig. S3, SD). These were attributed to (1) the charge transfer process due to aluminum oxidation and oxygen reduction, and (2) the impedance response due to the aluminum oxides/hydroxides corrosion products (Ref 38, 44). At low frequency (mHz region), the impedance diagrams showed dispersion, indicating instability of the system caused by the pitting

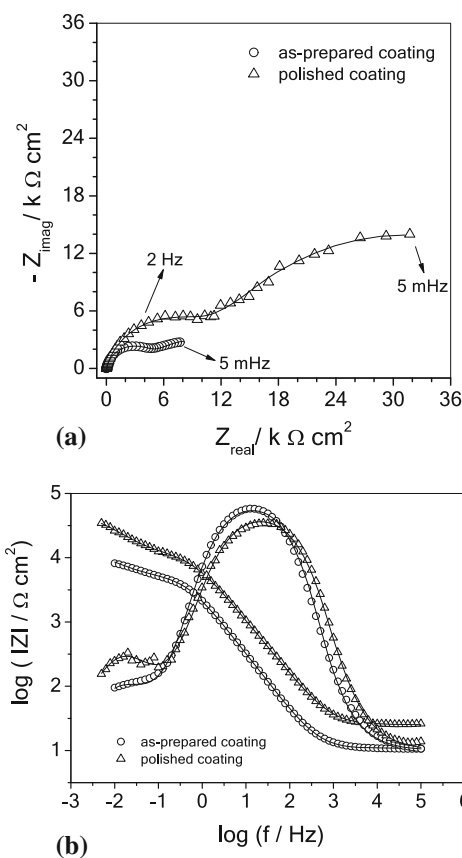


Fig. 13 (a) Complex plane and (b) Bode phase plots for Al coatings at ~ 70 h of immersion in 3.5 wt.% NaCl solution at 25 °C. The symbols correspond to the experimental data, and the solid lines are the fits

development (Fig. S3, SD). The Bode ϕ versus $\log(f)$ plots showed a large minimum with the peak at 25 Hz and a phase angle of around -80° , which is typical of a capacitive response. In the low-frequency region (< 0.1 Hz), the $|Z|$ values tended to increase as the frequency decreased, suggesting a diffusion contribution (Ref 38).

For the coatings at ~ 70 h and ~ 500 h of immersion (Figs. 13a, 14a), the Nyquist plots showed two separated semicircles, with the amplitude of the semicircles being greater for the polished coating compared to the as-prepared one. Accordingly, the polished coating showed the highest $|Z|$ value (Figs. 13b, 14b), suggesting that removal of the top layer diminished both the defects at the surface and the corrosion process due to the precipitation of corrosion products on the active areas (Ref 18, 29). As expected, the as-prepared coating presented the lowest $|Z|$ value (Figs. 13b, 14b), consistent with a more severe pitting attack, together with increased defects and pores that were filled with electrolyte (Ref 32, 45). For both the as-prepared and polished coatings, the $|Z|$ values at $f < 0.1$ Hz tended to increase as the frequency decreased, as explained

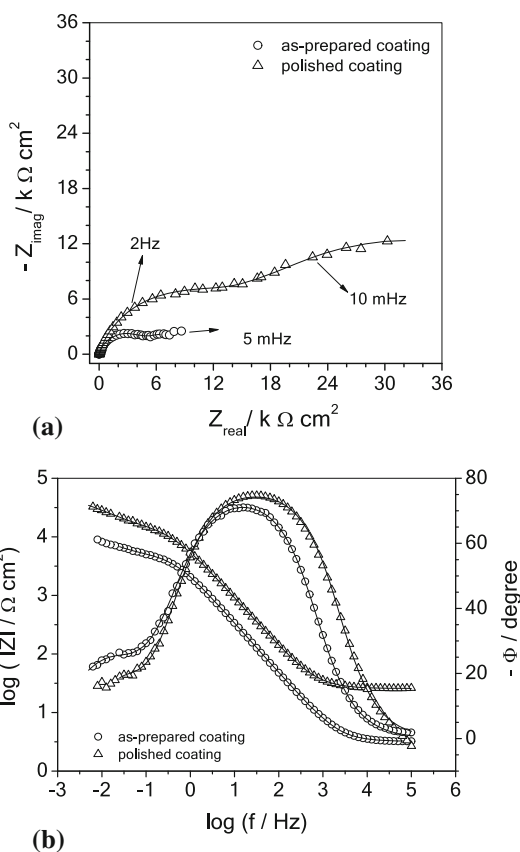


Fig. 14 (a) Complex plane and (b) Bode phase plots for Al coatings at ~ 500 h of immersion in 3.5 wt.% NaCl solution at 25 °C. The symbols correspond to the experimental data, and the solid lines are the fits

above, in agreement with the literature (Ref 18). The Bode plots at medium–high frequencies (MF–HF) showed one asymmetric time constant, suggestive of the presence of two overlapped time constants. The differences between the diagrams were a slightly higher phase angle and larger frequency region for the polished coating, indicating a higher capacitive system. As reported previously (Ref 18, 46, 47) for CGS aluminum coatings, the impedance response at MF–HF region shows two partially overlapped time constants: one at higher frequency attributed to aluminum oxidation (Al to Al^+ and Al^+ to Al^{3+} (Ref 39) and oxygen reduction and other at $f < 0.1$ Hz assigned to the dissolution/precipitation of corrosion products and diffusion of ions through a deteriorated barrier layer.

The qualitative analysis was confirmed by quantitative interpretation of the EIS data obtained for the coated samples at different immersion times, using the electrical equivalent circuit (EEC), as shown in Fig. 15. Chi-squared (χ^2) values of around 10^{-4} together with errors $< 10\%$ for each parameter (Table S1, SD) and the good agreement between the fitted and experimental impedance diagrams (Figs. 11, 12) indicated the suitability of the selected EEC

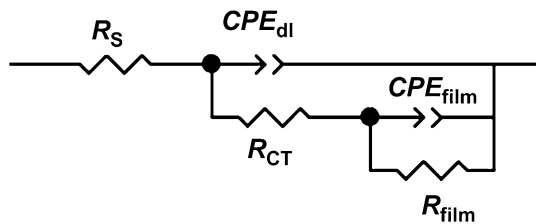


Fig. 15 Equivalent electrical circuits used to fit the EIS data for the substrate and the Al coatings

(Fig. 15), as suggested previously by EEC (Ref 18, 48). Fitting of the experimental data was not performed for the substrate, due to the dispersion of the data at low frequency ($f < 1$ Hz).

The parameter R_s is the uncompensated solution resistance. The constant phase element (CPE) used in the equivalent circuit is composed by two components: $CPE-T$ that is the admittance, which is proportional to the capacitance, and $CPE-P$ or n the exponent. The constant phase element represents a non-ideal capacitor, which means a resistance when the exponent $n = 0$, an ideal capacitor ($n = 1$), a Warburg impedance ($n = 0.5$), an ideal inductor ($n = -1$) (Ref 49). Values of n in the range $0.6 < n < 1$ are related to the heterogeneous charge distribution at the surface or heterogeneous distribution of the properties inside the coating (Ref 50). The CPE_{dl}/R_{ct} sub-circuit represents the constant phase element related to the electric double layer (CPE_{dl}) and the charge transfer resistance (R_{ct}) due to the anodic and cathodic processes: oxidation of the matrix (Al and/or Mg) and reduction of oxygen from the solution. CPE_{film}/R_{film} sub-circuit represents the constant phase element (CPE_{film}) of the aluminum oxide in parallel with the resistance (R_{film}) that comprises the resistance of the oxide film/products of corrosion and the resistance of the solution inside the pores.

The polished coating showed R_{ct} of around $38 \text{ k}\Omega \text{ cm}^2$ until 300 h (Fig. 16a), followed by an increase to $55 \text{ k}\Omega \text{ cm}^2$ up to 350 h and then a decrease and stabilization at around $37 \text{ k}\Omega \text{ cm}^2$ for $t > 700$ h. The increase of R_{ct} was due to the increase in aluminum corrosion products on the active regions (Ref 18). As the time lapses, the dissolution and porosity of the corrosion products led to lower the R_{ct} values (Ref 18).

For the as-prepared coating, the R_{ct} values oscillated between 2 and $12 \text{ k}\Omega \text{ cm}^2$ from 1 h to 600 h of immersion. This oscillation was attributed to the presence of pores that could block/unblock the formation/dissolution of corrosion products. From 600 h to 800 h, R_{ct} increased to $30 \text{ k}\Omega \text{ cm}^2$ probably due to the accumulation of hydrolysis products of aluminum ions on the active regions and then drastically decreased, due to the attack on the coating/substrate interface and the formation of a galvanic couple between the aluminum alloy and the Al coating. As shown in Fig. 9,

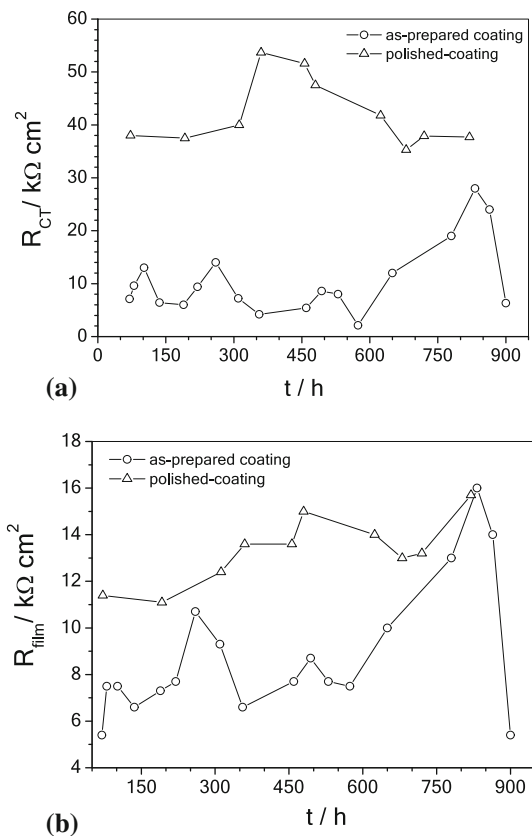


Fig. 16 (a) R_{ct} and (b) R_{film} for the Al-based coatings in 3.5 wt.% NaCl solution at 25 °C, according to time

the coating/substrate cross section was extensively damaged, with pathways through the coating that allowed the electrolyte to reach the substrate.

For the polished coating, the R_{film} values increased with immersion time, reaching around $16 \text{ k}\Omega \text{ cm}^2$ at the end of the experiments (Fig. 16b). For the as-prepared coating, the R_{film} values were $5 \text{ k}\Omega \text{ cm}^2$ at 1 h and increased to $11 \text{ k}\Omega \text{ cm}^2$ at 300 h, then decreased to $7 \text{ k}\Omega \text{ cm}^2$ at 350 h, increased again to $16 \text{ k}\Omega \text{ cm}^2$ up to 800 h and then decreased abruptly to $5 \text{ k}\Omega \text{ cm}^2$. The increase in this resistance during the initial period was associated with the increase in the film thickness, while decreases were due to the increased porosity of the film, especially surrounding the undissolved larger aluminum particles. Further increase in the film resistance was caused by blocking of the pores by the corrosion products. The different behaviors of R_{film} at the end of the experiments ($t > 800$ h) for the as-prepared and polished samples could be explained considering that the electrolyte completely damaged the coating/substrate interface of the as-prepared material extending the corrosion process to the substrate while only some regions of the polished coating/substrate interface were reached by the electrolyte, while the coating/substrate interface of the

as-prepared material was completely damaged with corrosion of the substrate occurring (Fig. 9).

These studies demonstrated that the mechanical and morphological properties are in line with the corrosion results, both indicating the worst performance of the top layer compared to the bottom layer, which can be attributed to the effect of the incoming particles on the top, and tamping effect on the bottom layer. The open-circuit potential and EIS measurements for both as-prepared and polished coatings showed that the electrolyte reached at coatings/substrate interface leading to corrosion of the substrate. On the other hand, metallic-based Al coatings are produced by in situ-assisted cold spraying techniques, for instance, in situ shot-peening-assisted cold spraying, and in situ micro-forging-assisted cold spraying showed improvement in the corrosion resistance and coatings with higher corrosion resistance compared to the coatings reported in this manuscript (Ref 51–53). Electrochemical studies of Ni coatings revealed that the fully dense Ni-coated AZ31B presents comparable corrosion performance with annealed bulk Ni in 3.5 wt.% NaCl aqueous solution (Ref 51). Furthermore, weight loss and decrease in electrochemical impedance of the coated samples after long-term tests were not detected suggesting that deterioration of corrosion protection for Ni coating did not occur (Ref 51). The in situ shot-peening-assisted cold spraying was also used to spray Al6061 coatings onto AZ31B magnesium alloy (Ref 52). The results showed that the technique can significantly enhance the plastic deformation and consequently cohesion of deposited Al6061 particles by enhanced accumulative tamping effect that improves the microstructure and corrosion resistance. As a result, the fully dense Al6061 coating deposited by in situ SP-assisted cold spraying can provide completely effective protection for the AZ31B magnesium material from corrosion (Ref 53). The deposition of Al-based coatings (pure Al, AA2219, AA6061) by in situ micro-forging-assisted cold spray process produces fully dense Al-based coatings with relatively lower corrosion resistance (Ref 53) than those described in the present work. After 1000-h immersion, the Al-based coatings still provide excellent corrosion protection for the AZ31B Mg alloy substrate. Besides, an increase in electrochemical impedance of the coated samples after long-term tests is observed, suggesting that a passive film can further improve the corrosion protection performance of the Al-based coatings (Ref 53).

Conclusions

The microstructural analyses showed total thicknesses of $309 \pm 12 \mu\text{m}$ for the as-prepared coating and $204 \pm 4 \mu\text{m}$ for the polished coating. The sliding wear tests showed an

adhesive mechanism and volume loss of $3.2 \times 10^{-4} \text{ mm}^3 \text{ N}^{-1} \text{ m}^{-1}$. The abrasive test showed a decrease in the wear rate for the polished coating due to the lower number of pores, interparticle spaces and the high hardness value of the bottom layer. The electrochemical results and the SEM images obtained for the as-prepared and polished coatings indicated that the electrolyte had reached the coating/substrate interface after 900 h in the chloride medium. The top layer of the as-prepared coating did not contribute to improve the corrosion resistance, due to its porous nature and the presence of irregular and small defects along the cross section. Consequently, the initial accelerated corrosion through the pores increased the chemical attack, enlarging the small defects and allowing substantial attack at the coating/substrate interface. The removal of the top layer decreased the initial corrosion rate of the surface, avoiding strong attack on the small defects and allowing the electrolyte to reach only some areas of the coating/aluminum alloy interface. As a general conclusion, the mechanical, morphological and electrochemical findings indicated that the top layer was detrimental to the lifetime of the coating.

Acknowledgments The authors thank CNPq (Conselho Nacional de Pesquisa, procs. 153177/2014-4 and 201325/2014-4), and CAPES (Coordenação de Aperfeiçoamento do Pessoal de Ensino Superior) for financial support and scholarships.

References

1. D. Dzhurinskiy, E. Maeva, E. Leshchinsky, and R.G. Maev, Corrosion Protection of Light Alloys Using Low Pressure Cold Spray, *J. Therm. Spray Technol.*, 2012, **21**(2), p 304-313
2. F. Andreatta, H. Terryn, and J.H.W. De Wit, Corrosion Behaviour of Different Tempers of AA7075 Aluminium Alloy, *Electrochim. Acta*, 2004, **49**, p 2851-2862
3. F. Andreatta, M.M. Lohrengel, H. Terryn, and J.H.W. De Wit, Electrochemical Characterisation of Aluminium AA7075-T6 and Solution Heat Treated AA7075 Using a Micro-Capillary Cell, *Electrochim. Acta*, 2003, **48**, p 3239-3247
4. E. McCafferty, Sequence of Steps in the Pitting of Aluminum by Chloride Ions, *Corros. Sci.*, 2003, **45**(7), p 1421-1438
5. C.K. Lee, C.S. Chang, A.H. Tan, C.Y. Yang, and S.L. Lee, Preparation of Electroless Nickel-Phosphorous-TiO₂ Composite Coating for Improvement of Wear and Stress Corrosion Cracking Resistance of AA7075 in 3.5% NaCl, *Key Eng. Mater.*, 2015, **656–657**, p 74-79
6. Z.-A. Khansha, M.R. Saeri, and S. Otraj, Study of Stress Corrosion Cracking of AA7075-T6 Aluminum Alloy by Chromate Coatings in Aerial Industry, *Indian J. Fundam. Appl. Life Sci.*, 2015, **5**, p 2231-6345
7. R.M. Bandeira, J. van Drunen, A.C. Garcia, and G. Tremiliosi-Filho, Influence of the Thickness and Roughness of Polyaniline Coatings on Corrosion Protection of AA7075 Aluminum Alloy, *Electrochim. Acta*, 2017, **240**, p 215-224
8. U. Tiringir, I. Milošev, A. Durán, and Y. Castro, Hybrid Sol–Gel Coatings Based on GPTMS/TEOS Containing Colloidal SiO₂ and

- Cerium Nitrate for Increasing Corrosion Protection of Aluminium Alloy 7075-T6, *J. Sol-Gel Sci. Technol.*, 2018, **85**(3), p 546-557
9. R.N. Raoelison, Y. Xie, T. Sapanathan, M.P. Planche, R. Kromer, S. Costil, and C. Langlade, Cold Gas Dynamic Spray Technology: A Comprehensive Review of Processing Conditions for Various Technological Developments till to Date, *Addit. Manuf.*, 2018, **19**, p 134-159
 10. V.K. Champagne, *The Cold Spray Materials Deposition Process Fundamentals and Applications*, Woodhead Publisher, Sawston, 2007
 11. E. Irissou, J. Legoux, A.N. Ryabinin, B. Jodoin, and C. Moreau, Review on Cold Spray Process and Technology: Part I—Intellectual Property, *J. Therm. Spray Technol.*, 2008, **17**, p 495-516
 12. X. Qiu, N.H. Tariq, J. Wang, J. Tang, L. Gyansah, Z. Zhao, and T. Xiong, Microstructure, Microhardness and Tribological Behavior of Al₂O₃ Reinforced A380 Aluminum Alloy Composite Coatings Prepared by Cold Spray Technique, *Surf. Coat. Technol.*, 2018, **350**, p 391-400
 13. C. Lee and J. Kim, Microstructure of Kinetic Spray Coatings: A Review, *J. Therm. Spray Technol.*, 2015, **24**(4), p 592-610
 14. X. Zhou, X. Wu, H. Guo, J. Wang, and J. Zhang, Deposition Behavior of Multi-Particle Impact in Cold Spraying Process, *Int. J. Min. Met. Mater.*, 2010, **17**(5), p 635-640
 15. R.N. Raoelison, Ch Verdy, and H. Liao, Cold Gas Dynamic Spray Additive Manufacturing Today: Deposit Possibilities, Technological Solutions and Viable Applications, *Mater. Des.*, 2017, **133**, p 266-287
 16. M.M. Sharma, T.J. Eden, and B.T. Golesich, Effect of Surface Preparation on the Microstructure, Adhesion, and Tensile Properties of Cold-Sprayed Aluminum Coatings on AA2024 Substrates, *J. Therm. Spray Technol.*, 2014, **24**(3), p 410-422
 17. S. Rech, A. Trentin, S. Vezzù, E. Vedelago, J.-G. Legoux, and E. Irissou, Different Cold Spray Deposition Strategies: Single- and Multi-Layers to Repair Aluminium Alloy Components, *J. Therm. Spray Technol.*, 2014, **6061**, p 1237-1250
 18. F.S. da Silva, J. Bedoya, S. Dosta, N. Cinca, I.G. Cano, J.M. Guilemany, and A.V. Benedetti, Corrosion Characteristics of Cold Gas Spray Coatings of Reinforced Aluminum Deposited onto Carbon Steel, *Corros. Sci.*, 2017, **114**, p 57-71
 19. S. Siddique, C.-X. Li, A.A. Bernussi, S.W. Hussain, and M. Yasir, Enhanced Electrochemical and Tribological Properties of AZ91D Magnesium Alloy via Cold Spraying of Aluminum Alloy, *J. Therm. Spray Technol.*, 2019, **28**, p 1-10
 20. S.R. Bakshi, D. Wang, T. Price, D. Zhang, A.K. Keshri, Y. Chen, D.G. McCartney, P.H. Shipway, and A. Agarwal, Microstructure and Wear Properties of Aluminum/Aluminum–Silicon Composite Coatings Prepared by Cold Spraying, *Surf. Coat. Technol.*, 2009, **204**, p 503-510
 21. O. Meydanoglu, B. Jodoin, and E.S. Kayali, Microstructure, Mechanical Properties and Corrosion Performance of 7075 Al Matrix Ceramic Particle Reinforced Composite Coatings Produced by the Cold Gas Dynamic Spraying Process, *Surf. Coat. Technol.*, 2013, **235**, p 108-116
 22. S.R. Bakshi, T. Laha, K. Balani, A. Agarwal, and J. Karthikeyan, Effect of Carrier Gas on Mechanical Properties and Fracture Behaviour of Cold Sprayed Aluminium Coatings, *Surf. Eng.*, 2007, **23**, p 18-22
 23. Z. Zhang, F. Liu, E.-H. Han, L. Xu, and P.C. Uzoma, Effects of Al₂O₃ on the Microstructures and Corrosion Behavior of Low-Pressure Cold Gas Sprayed Al 2024-Al₂O₃ Composite Coatings on AA 2024-T3 Substrate, *Surf. Coat. Technol.*, 2019, **370**, p 53-68
 24. W.S. Tait, *An Introduction to Electrochemical Corrosion Testing for Practicing Engineers and Scientists*, Pair ODocs, Wisconsin, 1994
 25. A.C. Hall, L.N. Brewer, and T.J. Roemer, Preparation of Aluminum Coatings Containing Homogenous Nanocrystalline Microstructures Using the Cold Spray Process, *J. Therm. Spray Technol.*, 2008, **17**(3), p 352-359
 26. F.S. da Silva, N. Cinca, S. Dosta, I.G. Cano, J.M. Guilemany, and A.V. Benedetti, Cold Gas Spray Coatings: Basic Principles Corrosion Protection and Applications, *Eclat. Quim. J.*, 2017, **42**(1), p 09-32
 27. A. Moridi, S.M. Hassani-Gangaraj, M. Guagliano, and M. Dao, Cold Spray Coating: Review of Material Systems and Future Perspectives, *Surf. Eng.*, 2014, **30**(6), p 369-395
 28. S. Yin, P. Cavaliere, B. Aldwell, R. Jenkins, H. Liao, W. Li, and R. Lupoi, Cold Spray Additive Manufacturing and Repair: Fundamentals and Applications, *Addit. Manuf.*, 2018, **21**, p 628-650
 29. N.M. Chavan, B. Kiran, A. Jyothirmayi, P.S. Phani, and G. Sundararajan, The Corrosion Behavior of Cold Sprayed Zinc Coatings on Mild Steel Substrate, *J. Therm. Spray Technol.*, 2013, **22**(4), p 463-470
 30. M.R. Rokni, C.A. Widener, and V.R. Champagne, Microstructural Evolution of 6061 Aluminum Gas-Atomized Powder and High-Pressure Cold-Sprayed Deposition, *J. Therm. Spray Technol.*, 2013, **23**(3), p 514-524
 31. X. Zhou and P. Mohanty, Electrochemical Behavior of Cold Sprayed Hydroxyapatite/titanium Composite in Hanks' Solution, *Electrochim. Acta*, 2012, **65**, p 134-140
 32. Y. Tao, T. Xiong, C. Sun, L. Kong, X. Cui, T. Li, and G.L. Song, Microstructure and Corrosion Performance of a Cold Sprayed Aluminium Coating on AZ91D Magnesium Alloy, *Corros. Sci.*, 2010, **52**(10), p 3191-3197
 33. C.-J. Li and W.-Y. Li, Deposition Characteristics of Titanium Coating in Cold Spraying, *Surf. Coat. Technol.*, 2003, **167**, p 278-283
 34. E. Avcu, The Influences of ECAP on the Dry Sliding Wear Behaviour of AA7075 Aluminium Alloy, *Tribol. Int.*, 2017, **110**, p 173-184
 35. A.P. Sannino and H.J. Rack, Dry Sliding Wear of Discontinuously Reinforced Aluminum Composites: Review and Discussion, *Wear*, 1995, **189**(1–2), p 1-19
 36. S. Dosta, M. Couto, and J.M. Guilemany, Cold Spray Deposition of a WC-25Co Cermet onto Al7075-T6 and Carbon Steel Substrates, *Acta Mater.*, 2013, **61**(2), p 643-652
 37. N. Birbilis and R.G. Buchheit, Electrochemical Characteristics of Intermetallic Phases in Aluminum Alloys, *J. Electrochem. Soc.*, 2005, **152**(4), p B140-B151
 38. S. Lameche-Djeghaba, A. Benchettara, F. Kellou, and V. Ji, Electrochemical Behaviour of Pure Aluminium and Al–5%Zn Alloy in 3% NaCl Solution, *Arab. J. Sci. Eng.*, 2013, **39**(1), p 113-122
 39. F.S. da Silva, N. Cinca, S. Dosta, I.G. Cano, J.M. Guilemany, and A.V. Benedetti, Influence of Cold Gas Spray Parameters on the Corrosion Resistance of Al-Al₂O₃ Coatings Sprayed on Carbon Steel, *Corros. Eng. Sci. Technol.*, 2019, **54**(7), p 567-574
 40. Z. Jing and K. Dejun, Microstructures and Salt Spray Corrosion Behaviors of Cold Sprayed Al Coatings on S355 Steel in Marine Environment, *Surf. Rev. Lett.*, 2018, **25**(06), p 1-15
 41. R. Huang, M. Sone, W. Ma, and H. Fukunuma, The Effects of Heat Treatment on the Mechanical Properties of Cold-Sprayed Coatings, *Surf. Coatings Technol.*, 2015, **261**, p 278-288
 42. N.M. Chavan, B. Kiran, A. Jyothirmayi, P.S. Phani, and G. Sundararajan, The Corrosion Behavior of Cold Sprayed Zinc Coatings on Mild Steel Substrate, *J. Therm. Spray Technol.*, 2013, **22**, p 463-470
 43. W. Suna, A.W.Y. Tan, I. Marinescu, W.Q. Toh, and E. Liu, Adhesion, Tribological and Corrosion Properties of Cold-Sprayed CoCrMo and Ti6Al4V Coatings on 6061-T651 Al Alloy, *Surf. Coatings Technol.*, 2017, **326**, p 291-298

44. R. Krishnakumar and Z. Szklarska-Smialowska, Optical and Impedance Characteristics of Passive Films on Pure Aluminium, *Mater. Sci. Forum*, 1992, **111–112**, p 565-580
45. Y. Bai, Z.H. Wang, X.B. Li, G.S. Huang, C.X. Li, and Y. Li, Corrosion Behavior of Low Pressure Cold Sprayed Zn–Ni Composite Coatings, *J. Alloys Compd.*, 2017, **719**, p 194-202
46. S.E. Frers, M.M. Stefenel, C. Mayer, and T. Chierchie, AC-Impedance Measurements on Aluminium in Chloride Containing Solutions and Below the Pitting Potential, *J. Appl. Electrochem.*, 1990, **20**(6), p 996-999
47. H.J.W. Lenderink, M.V.D. Linden, and J.H.W. De Wit, Corrosion of Aluminium in Acidic and Neutral Solutions, *Electrochim. Acta*, 1993, **38**(14), p 1989-1992
48. Q.J. Zhu, K. Wang, X.H. Wang, and B.R. Hou, Electrochemical Impedance Spectroscopy Analysis of Cold Sprayed and Arc Sprayed Aluminium Coatings Serviced in Marine Environment, *Surf. Eng.*, 2012, **28**(4), p 300-305
49. M.E. Orazem and B. Tribollet, *Electrochemical Impedance Spectroscopy*, 1st ed., Wiley, New York, 2008
50. B. Hirschorn, M.E. Orazem, B. Tribollet, V. Vivier, I. Frateur, and M. Musiani, Constant-Phase-Element Behavior Caused by Resistivity Distributions in Films, *J. Electrochem. Soc.*, 2010, **157**(12), p C458
51. Y.-K. Wei, Y.-J. Li, Y. Zhang, X.-T. Luo, and C.-J. Li, Corrosion Resistant Nickel Coating with Strong Adhesion on AZ31B Magnesium Alloy Prepared by an In Situ Shot-Peening-Assisted Cold Spray, *Corros. Sci.*, 2018, **138**, p 105-115
52. Y.-K. Wei, X.-T. Luo, C.-J. Li, and C.-X. Li, Optimization of In-Situ Shot-Peening-Assisted Cold Spraying Parameters for Full Corrosion Protection of Mg Alloy by Fully Dense Al-Based Alloy Coating, *J. Therm. Spray Technol.*, 2017, **26**(1–2), p 173-183
53. Y.-K. Wei, X.-T. Luo, Y. Ge, X. Chu, G.-S. Huang, and C.-J. Li, Deposition of Fully Dense Al-Based Coatings via In Situ Micro-forging Assisted Cold Spray for Excellent Corrosion Protection of AZ31B Magnesium Alloy, *J. Alloys Compd.*, 2019, **806**, p 1116-1126

Publisher's Note Springer Nature remains neutral with regard to jurisdictional claims in published maps and institutional affiliations.